Consistent hybrid finite volume/element formulations: model and complex viscoelastic flows

M. S. Chandio, K. S. Sujatha and M. F. Webster*,†

Institute of non-Newtonian Fluid Mechanics, Department of Computer Science, University of Wales Swansea, Singleton Park, SA2 8PP, Swansea, U.K.

SUMMARY

The accuracy and consistency of a new cell-vertex hybrid finite element/volume scheme are investigated for viscoelastic flows. Finite element (FE) discretization is employed for the momentum and continuity equation, with finite volume (FV) applied to the constitutive law for stress. Here, the interest is to explore the consequences of utilizing conventional cell-vertex methodology for an Oldroyd-B model and to demonstrate resulting drawbacks in the presence of complex source terms on structured and unstructured grids. Alternative strategies worthy of consideration are presented. It is demonstrated how high-order accuracy may be achieved in steady state by respecting consistency in the formulation. Both FE and FV spatial discretizations are embedded in the scheme, with FV triangular sub-cells referenced within parent triangular finite elements. Both model and complex flow problems are selected to quantify and assess accuracy, appealing to analysis and experimental validation. The test problem is that of steady sink flow, a pure extensional flow, which reflects some of the numerical difficulties involved in solving more generalized viscoelastic flows, where both source and flux terms may contribute equally to stress propagation. In addition, a complex transient filament-stretching flow is chosen to compute the evolution of stress fields within liquid bridges. Shortcomings of the various stress upwinding schemes are discussed in this context, whilst dealing with such free-surface type problems. Here, stress fluctuation distribution alone is advocated, and a Lax-scheme is found to deliver accuracy and stability to the computational results, comparing well with the literature. Copyright © 2004 John Wiley & Sons, Ltd.

KEY WORDS: cell-vertex finite volume; consistency; viscoelastic; filament-stretching; Lax–Wendroff; fluctuation distribution

1. INTRODUCTION

Finite volume (FV) high-resolution upwind methods for hyperbolic conservation laws and their extensions have been the subject of intensive research for more than half a century, with remarkable advances in the last two decades or so [1–12]. These methods have now reached a stage of maturity and play a central role in numerical discretization of differential equation systems. The FV approach may be viewed as a 'method of moments' FE formulation, with

---

*Correspondence to: M. F. Webster, Institute of non-Newtonian Fluid Mechanics, Department of Computer Science, University of Wales Swansea, Singleton Park, SA2 8PP, Swansea, U.K.
†E-mail: m.f.webster@swan.ac.uk

weighting functions taken as unity. Literature of relevance here falls into two categories, those with complete FV implementations [2] and those of hybrid form [1, 9, 11, 12]. Early numerical simulations for viscoelastic fluids were performed using FE Galerkin discretization in conjunction with upwinding techniques (Streamline-unwinding, SU, streamline upwinding Petrov–Galerkin, SUPG) [10, 13]. In the FV domain, considerable progress has been made for pure advection equations [3, 8] and has sufficiently advanced to accommodate viscoelastic flows, where source terms may play a dominant role.

The contributions of Crumpton *et al.* [5], Struijs *et al.* [8] are worthy of mention. These works have implemented cell-vertex FV formulations for compressible Navier–Stokes, Euler and advection equations, respectively. On triangles, Berzins and Ware [7] concentrated on a cell-centred FV approach. The distinction between cell-centred and cell-vertex schemes lies in the level of auxiliary interpolation and the upwinding techniques appropriate for each. In cell-centred methods, solution variables are positioned at the centroids of the control volume. In contrast, cell-vertex methods use the mesh points to locate solution variables.

Sato and Richardson [9] employed a time-explicit FE-method on the momentum equation and time-implicit FV-method for pressure and stress, of cell-centred type. In order to achieve high-order upwinding, a total variational diminishing flux corrected transport (TVD-FCT) schemes was applied to the advection terms of the constitutive equation. Darwish and Whiteman [2] implemented a staggered grid-FV method, and Crumpton *et al.* [5] developed a cell-vertex FV method on structured quadrilateral and hexahedral meshes for Navier–Stokes equations.

Features of the current hybrid approach include a time-stepping procedure that combines a finite element discretization (semi-implicit second-order/pressure correction) for continuity and momentum equations, with a cell-vertex finite volume scheme for stress. This effective combination is employed as a fractional-staged formulation within each time-step. An individual parent finite element triangular cell is divided into four finite-volume triangular sub-cells. Interpolation on the parent-*fe*-cell is quadratic in velocity, linear in pressure. On the sub-cell, interpolation is linear only. An important aspect of the discretization is that with stress variables located at the vertices of the finite volume cells, no interpolation is required to recover the finite element nodal stress values.

Under *fv*-discretization and to date, various forms of fluctuation splitting schemes have been considered, and their properties analysed [14]. In this regard, our prior studies have established accuracy properties against analytical solutions for smooth flows [14], and some non-smooth flows [1]. The relative strengths and weaknesses of various strategies for dealing with flux and source terms have been identified. In the above cases, the hybrid FE/FV scheme is found to produce second-order accurate and efficient solutions to viscoelastic flows. There is reduction in loss of accuracy (by up to one order) with the hybrid FE/FV form compared to the FE/SUPG scheme. Compared to the FE/SUPG method, the hybrid FE/FV alternative requires smaller time steps, less iterations and less CPU time per iteration. These advantages offer the possibility of improved efficiency for larger problems with this hybrid FE/FV scheme.

In the present study, our attention is focused mainly on the contrast between consistent and inconsistent treatments for source and flux terms within cell-vertex finite volume formulations. Consistent and inconsistent schemes are compared in our precursor work on model problems. The inconsistent approach provides inaccurate results, even for simple model problems. This has been demonstrated on channel flow, for example, where such schemes have been shown to lack stability [14]. The consistent approach has performed well in terms of stability. It has

provided second-order accuracy for steady-state model problems. In contrast, here a model sink flow problem is chosen to quantify accuracy and consistency, addressing both structured and unstructured meshing. Once, this is established, the proposed hybrid FE/FV method is employed on a complex viscoelastic flow with free-surface. The drawbacks of various FV implementations are discussed. Here, specifically we address filament-stretching for viscoelastic fluids, focusing upon constant shear-viscosity fluid properties. It is appropriate to consider fluid representation through the Oldroyd-B model [27], for which we adopt a high-polymeric viscosity contribution. Here, we discuss the break-up of viscoelastic liquid-bridges under elongation, where the stretching of the liquid-bridge is confined between two end-plates. Such a setting may be used in rheometry to measure the elongational viscosity of a fluid [15]. Over the preceding decade, much interest has been expressed in the area of extensional rheology for polymer solutions [16–19]. In this regard, the filament-stretching rheometer, introduced by Tritaatmadja and Sridhar [15], has proved to be a useful experimental tool. The primary goal of these studies has been to determine the nature of deformation in the central portion of the filament. This detects if the flow approaches ideal uniaxial elongation and leads to the observation of rheological properties, that either enhance or restrain ideal uniaxial deformation.

Finite element simulations for viscous and viscoelastic fluids within filament-stretching flows have been performed extensively in the literature, see References [16–19]. A detailed literature review on this problem is presented in our precursor work [20]. While employing the full FE scheme (FE/SUPG), to solve this complex problem, τ_{zz} decreases with time sustaining negative solution values. Here, no contribution (in the weighting function) is made to the nodes in the free-surface region, due to the inward pointing direction of the velocity. In contrast, the hybrid FE/FV Lax–Wendroff scheme has furnished comparable results with those from the literature. In this work, we propose the appropriate finite volume scheme to be employed to model such complex flow problems. We illustrate the differences between fluctuation distribution and median-dual-cell constructs, within a cell-vertex discretization on structured and unstructured triangular meshes. Also, various fluctuation distribution schemes, namely, Ldb, Psi and Lax–Wendroff, are contrasted in this study.

2. GOVERNING EQUATIONS

The governing equations for incompressible, viscoelastic flows are represented by conservation laws for mass and momentum, in conjunction with an equation of state for stress. Posed in non-dimensional form, the balance equations under isothermal flow conditions may be expressed as

$$\nabla . \mathbf{u} = 0 \tag{1}$$

$$Re \frac{\partial \mathbf{u}}{\partial t} = -Re \, \mathbf{u}.\nabla \mathbf{u} - \nabla p + \nabla . \left(2 \frac{\mu_s}{\mu_0} \mathbf{d} + \tau \right) \tag{2}$$

and the constitutive equation for an Oldroyd-B fluid may be expressed as

$$We \frac{\partial \tau}{\partial t} = - We \mathbf{u}.\nabla \tau - \tau + 2 \frac{\mu_e}{\mu_0} \mathbf{d} + We(\mathbf{L}.\tau + \tau.\mathbf{L}^\dagger) \tag{3}$$

where $\mathbf{u}$, p, $\boldsymbol{\tau}$ represent the fluid velocity, the hydrodynamic pressure and the extra-stress tensor. The total viscosity μ_0 is split into solvent (μ_s) and polymeric (μ_e) contributions, such that $\mu_0 = \mu_s + \mu_e$; $\mathbf{d} = (\mathbf{L} + \mathbf{L}^{\dagger})/2$ represents the Euler rate-of-deformation tensor and $\mathbf{L}^{\dagger} = \nabla.\mathbf{u}$, the velocity gradient. The non-dimensional variables, namely, velocity, pressure, length, stress and time may be expressed as

$$u^* = \frac{u}{U}, \quad p^* = \frac{L}{\mu_0 U}\,p, \quad x^* = \frac{x}{L}, \quad \tau^* = \frac{L}{\mu_0 U}\,\tau, \quad \mu^* = \frac{\mu}{\mu_0}, \quad t^* = t\,\frac{L}{U} \tag{4}$$

The Reynolds and Weissenberg numbers are defined as

$$Re = \frac{\rho U L}{\mu_0}, \quad We = \frac{\lambda U}{L} \tag{5}$$

where ρ, λ are the fluid density and relaxation time and U, L are characteristic velocity and length scale of the flow. The zero shear-rate viscosity (constant) is taken as the characteristic scale for viscosity.

3. THE HYBRID FINITE ELEMENT/FINITE VOLUME METHOD

The finite element grid is used as a platform for the finite volume grid, from which control volumes are constructed. Each FV cell is a sub-triangle resulting from a parent FE cell, see Figure 1(a). The unique subtended median-dual-cell zone (mdc), around a particular node l, surrounded by FV sub-cells T, is illustrated in Figure 1(b). The six-noded parent FE cell is based on a triangular cell with three vertices and three mid-side nodes. Velocity interpolation is achieved via quadratic shape functions, using the six nodal values, and the pressure by linear functions based upon the vertices alone. The stresses are computed on the vertices of the FV cells as outlined below.
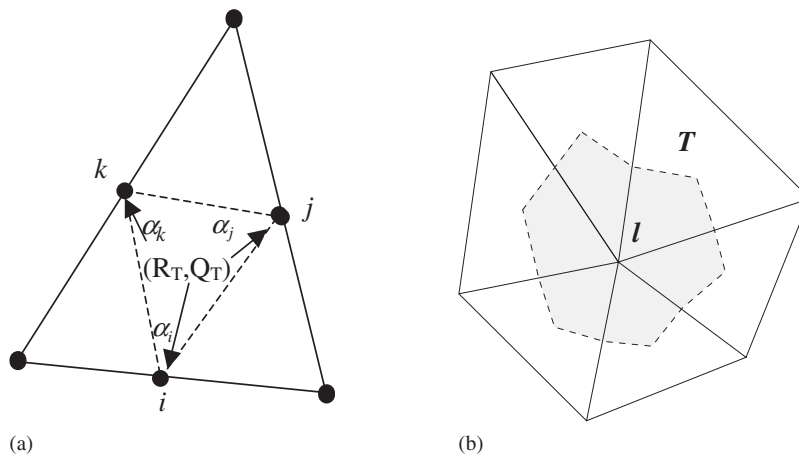

Figure 1. (a) FE with four FV sub-cells; and (b) mdc area for node l.

First, we recast the stress constitutive equation (3) in conservative form,

$$\frac{\partial \boldsymbol{\tau}}{\partial t} + \nabla.\boldsymbol{R} = \boldsymbol{Q} \tag{6}$$

where the flux $\boldsymbol{R}$ and source $\boldsymbol{Q}$ can be defined as

$$\boldsymbol{R} = \mathbf{u}\boldsymbol{\tau} \tag{7}$$

$$\boldsymbol{Q} = \frac{1}{We}\left(2\,\frac{\mu_e}{\mu_0}\,\mathbf{d} - \boldsymbol{\tau} + (\mathbf{L}.\boldsymbol{\tau} + \boldsymbol{\tau}.\mathbf{L}^{\dagger})\right) \tag{8}$$

Velocity gradients are represented via recovery procedures [13]. It is common practice to refer to a single scalar component τ of stress, with correspondence in flux and source terms. In the presence of source terms, the standard treatment advocate widely in the literature consists in dealing separately with the flux and source terms (inconsistent approach). Here, in contrast, a new formulation is proposed, whereby both flux and source terms are evaluated in a consistent manner.

3.1. Inconsistent fv-nodal update

Here, the fluxes are distributed using α_l^T-FD coefficients on the whole FV cell area, whereas the control volume for the source term, the mdc, is one-third that of the FV cell area. Hence, this formulation is inconsistent, both in respect of control volume usage and reference to α_l^T-FD coefficients.

$$\hat{\Omega}_l\,\frac{\tau_l^{n+1} - \tau_l^n}{\Delta t} = \alpha_l^T R_T + Q_{\mathrm{mdc}} \tag{9}$$

where R_T is the integral of the flux (R) over triangle T (see Equations (26) and (27)), and Q_{mdc} is the source associated with node l taken over the area of the surrounding mdc, $(Q_{\mathrm{mdc}} = \int_{\Omega_{\mathrm{mdc}}} Q\,\mathrm{d}\Omega_{\mathrm{mdc}})$, respectively. Here, the Ldb scheme is employed for the evaluation of α_l^T-FD coefficients.

3.2. Consistent fv-nodal update

Here, both fluxes are sources are distributed alike using α_l^T-FD coefficients on the whole FV cell area,

$$\hat{\Omega}_l\,\frac{\tau_l^{n+1} - \tau_l^n}{\Delta t} = \sum_{\forall T}\alpha_l^T(R_T + Q_T) \tag{10}$$

The notation $\sum_{\forall T}$, represents summation over contribution from all FV-cells (T) surrounding node l, and $\hat{\Omega}_l$ the area of the median dual cell (mdc) associated with node l. In addition, we have FD-factors α_l^T, temporal stress τ_l^T at node l, and {flux R_T, source Q_T} contributions on FV-triangle, T $(Q_T = \int_{\Omega_T} Q\,\mathrm{d}\Omega_T)$. Here, both Ldb and Psi schemes are used for the evaluation of α_l^T-FD coefficients. The scheme following stencil (10) is consistent both in α_l^T-FD coefficient application and control volume.

3.2.1. Hybrid combinations. Results are obtained by switching flux and source term treatment between Ldb and Psi schemes, to determine the influence of positivity upon the computations, and in particular its consistent application to flux terms. This is achieved through stencils of:

$$\overset{\wedge}{\Omega}_l \, \frac{\tau_l^{n+1} - \tau_l^n}{\Delta t} = \alpha_{l(\text{Ldb})}^T R_T + \alpha_{l(\text{Psi})}^T Q_T \tag{11}$$

$$\overset{\wedge}{\Omega}_l \, \frac{\tau_l^{n+1} - \tau_l^n}{\Delta t} = \alpha_{l(\text{Psi})}^T R_T + \alpha_{l(\text{Ldb})}^T Q_T \tag{12}$$

3.2.2. Median dual cell considerations. In order to retain stability at high *We* numbers, Aboubacar and Webster [11] and Webster *et al.* [12], improved the consistent approach (Equation (10)) by appealing to median dual cell contributions. Summing over all fv-subcells surrounding node *l* yields the CT_3-scheme, provides a generalized stencil:

$$\frac{\Delta \tau_l^{n+1}}{\Delta t} = \underbrace{\frac{\sum_{\forall T_l} \delta_T \alpha_l^T b_{T_l}}{\Omega_1}}_{\text{FD}} + \underbrace{\frac{\sum_{\forall \text{mdc}_l} \delta_{\text{mdc}}^T \alpha_{\text{mdc}}^T b_{\text{mdc}}^l}{\Omega_2}}_{\text{mdc}} \tag{13}$$

where $b_{T_l} = (R_T + Q_T)$, $b_{\text{mdc}}^l = (R_{\text{mdc}} + Q_{\text{mdc}})^l$, and appealing to $\Omega_{\text{FD}} = \sum_{T_l} \delta_T \alpha_l^T \Omega_{T_l}$, and $\Omega_{\text{mdc}} = \sum_{\text{mdc}_l} \delta_{\text{mdc}}^T \Omega_l^{T_l}$. Theoretically, δ_T and δ_{mdc} are mutually linked and complementarily exclusive. Blending FD and *mdc* contributions with parameters δ_T and δ_{mdc} provides various alternative scheme combinations (CT_0, CT_2, CT_3 see References [11, 12]). These may be categorized in a generalized manner, around area weighting factors Ω_1 and Ω_2, and blending parameters, δ_T, and δ_{mdc}. We obtain the CT_3-scheme by setting $\Omega_1 = \Omega_2 \equiv \Omega_{\text{FD}} + \Omega_{\text{mdc}}$; alternatively, we can recover the CT_2-scheme with the combination $\Omega_1 = \Omega_{\text{FD}}$ and $\Omega_2 = \Omega_{\text{mdc}}$; the original nodal-update (CT_0) corresponds to $\Omega_1 = \Omega_2 \equiv \hat{\Omega}_l$.

Fluctuation distribution coefficients α_l^T, may be provided via an appropriate choice of scheme, for example, Ldb or Psi. Both such options offer second-order accuracy at steady state. Wapperom and Webster [1], recommended setting of blending factors as $\delta_T = \kappa$ and $\delta_{\text{mdc}} = 1$, with $\kappa = \xi/3$ if $|\xi \leqslant 3|$ and 1 otherwise. Here, $\xi = We\,(\mathbf{a}/h)$, with $\mathbf{a}$ the magnitude of an advection velocity per FV-cell and h the square-root of the area of the FV-cell in question. With the above parameter combinations (so $\delta_{\text{mdc}} = 1$), both CT_2 and CT_0 variants proved inadequate in tracking transient solution evolution in a start-up planar Poiseuille flow. In particular, the CT_2-scheme was sensitive to the setting of δ_{mdc}. There, significant improvement in transient accuracy was achieved with the CT_2-scheme by appealing to a dynamic δ_{mdc} factor setting in the form, $\delta_{\text{mdc}} = 1 - \delta_T$. In contrast, the CT_3-scheme was relatively insensitive to δ_{mdc} setting, as it encompasses consistent treatment of control-volumes for flux and source terms on the r.h.s., and consistent area-weighting for time-terms on the l.h.s. of the equation. Hence, this is the preferred option of choice.

4. NUMERICAL ALGORITHM

We outline the structure of the FE scheme, and point to the hybrid FE/FV options in contrast, referring to Matallah *et al.* [13] and Wapperom and Webster [1] for detailed discussion. The

general framework is a time-splitting semi-implicit formulation, involving two distinct aspects: a Taylor–Galerkin scheme and a pressure-correction scheme. The Taylor–Galerkin scheme is a two-step Lax–Wendroff time stepping procedure, extracted via a Taylor series expansion in time [13]. The pressure-correction method accommodates the incompressibility constraint to ensure second-order accuracy in time, with pressure-splitting factor $\theta = \frac{1}{2}$. A three-stage structure emerges per time step, that may be expressed in semi-discrete form

Stage 1a: $\quad \dfrac{2Re}{\Delta t}(\boldsymbol{U}^{n+(1/2)} - \boldsymbol{U}^n) = [\nabla.(2\mu_2\boldsymbol{D} + \boldsymbol{T}) - Re\,\boldsymbol{U}.\nabla\boldsymbol{U} - \nabla p]^n$

$\qquad\qquad \dfrac{2We}{\Delta t}(\boldsymbol{T}^{n+(1/2)} - \boldsymbol{T}^n) = [2\mu_1\boldsymbol{D} - \boldsymbol{T} - We\{\boldsymbol{U}.\nabla\boldsymbol{T} - \boldsymbol{T}.\nabla\boldsymbol{U} - (\boldsymbol{T}.\nabla\boldsymbol{U})^+\}]^n$

Stage 1a: $\quad \dfrac{Re}{\Delta t}(\boldsymbol{U}^* - \boldsymbol{U}^n) = [\nabla.\boldsymbol{T} - Re\,\boldsymbol{U}.\nabla\boldsymbol{U}]^{n+(1/2)} + [\nabla.(2\mu_1\boldsymbol{D}) - \nabla p]^n$

$\qquad\qquad \dfrac{We}{\Delta t}(\boldsymbol{T}^{n+1} - \boldsymbol{T}^{n+(1/2)}) = [2\mu_1\boldsymbol{D} - \boldsymbol{T} - We\{\boldsymbol{U}.\nabla\boldsymbol{T} - \boldsymbol{T}.\nabla\boldsymbol{U}$

$\qquad\qquad\qquad\qquad\qquad\qquad\qquad\qquad\qquad - (\boldsymbol{T}.\nabla\boldsymbol{U})^+\}]^{n+(1/2)}$

$\hspace{11cm}$ (14a)

Stage 2: $\quad \nabla^2(p^{n+1} - p^n) = \dfrac{Re}{\theta\Delta t}\,\nabla.\boldsymbol{U}^*$

Stage 3: $\quad \dfrac{2Re}{\Delta t}(\boldsymbol{U}^{n+1} - \boldsymbol{U}^*) = -\theta\nabla(p^{n+1} - p^n)$

Upon spatial discretization, the above stages may be expressed as

Stage 1a: $\quad A_u^a(\boldsymbol{U}^{n+(1/2)} - \boldsymbol{U}^n) = b_u^a(p^n, \boldsymbol{U}^n, \boldsymbol{T}^n, \boldsymbol{D}^n)$

$\qquad\qquad \dfrac{2}{\Delta t} A_\tau(\boldsymbol{T}^{n+(1/2)} - \boldsymbol{T}^n) = b_\tau(\boldsymbol{U}^n, \boldsymbol{T}^n, \boldsymbol{D}^n)$

Stage 1b: $\quad A_u^b(\boldsymbol{U}^* - \boldsymbol{U}^n) = b_u^b(p^n, \boldsymbol{U}^n, \boldsymbol{U}^{n+(1/2)}, \boldsymbol{T}^{n+(1/2)}, \boldsymbol{D}^{n+(1/2)})$

$\hspace{11cm}$ (14b)

$\qquad\qquad \dfrac{1}{\Delta t} A_\tau(\boldsymbol{T}^{n+1} - \boldsymbol{T}^n) = b_\tau(\boldsymbol{U}^{n+(1/2)}, \boldsymbol{T}^{n+(1/2)}, \boldsymbol{D}^{n+(1/2)})$

Stage 2: $\quad A_2(p^{n+1} - p^n) = b_2(\boldsymbol{U}^*)$

Stage 3: $\quad A_3(\boldsymbol{U}^{n+1} - \boldsymbol{U}^*) = b_3(p^n, p^{n+1})$

where

$A_u^a = \dfrac{2Re}{\Delta t} M + \dfrac{\mu_2}{2} S, \quad b_u^a = \{\boldsymbol{F}_1 - [\mu_2 S + Re\,N(\boldsymbol{U})]\boldsymbol{U} - B_1\boldsymbol{T} + L^T P\}^n$

$A_u^b = \dfrac{Re}{\Delta t} M + \dfrac{\mu_2}{2} S, \quad b_u^b = \{\boldsymbol{F}_1 - [Re\,N(\boldsymbol{U})]\boldsymbol{U} - B_1\boldsymbol{T}\}^{n+(1/2)} + (L^T P + \mu_2 S)^n$

$A_2 = K, \quad b_2 = \dfrac{Re}{\theta\Delta t}\,L\boldsymbol{U}^*, \quad A_3 = \dfrac{2Re}{\Delta t} M, \quad \text{and} \quad b_3 = -\theta L^T(P^{n+1} - P^n)$

$\qquad\qquad$

Above, M, S, and $N(\boldsymbol{U})$ represent the consistent mass-matrix, the diffusion matrix and the advection matrix, respectively (D is represented via the diffusion matrix S). Throughout the problem domain Ω, these matrices are expressed as

$$M_{ij} = \int_\Omega \phi_i \phi_j \, \mathrm{d}\Omega, \quad N(\boldsymbol{U})_{ij} = \int_\Omega \phi_i (\phi_l \boldsymbol{U}_l) \nabla \phi_j \, \mathrm{d}\Omega$$

$$(S_{11})_{ij} = \int_\Omega \left\{ 2 \frac{\partial \phi_i}{\partial r} \frac{\partial \phi_j}{\partial r} + \frac{\partial \phi_i}{\partial z} \frac{\partial \phi_j}{\partial z} + \frac{2}{r} \phi_i \phi_j \right\} \mathrm{d}\Omega$$

$$(S_{12})_{ij} = (S_{21})_{ij} = \int_\Omega \left\{ \frac{\partial \phi_i}{\partial z} \frac{\partial \phi_j}{\partial r} \right\} \mathrm{d}\Omega \qquad (15)$$

$$(S_{22})_{ij} = \int_\Omega \left\{ 2 \frac{\partial \phi_i}{\partial z} \frac{\partial \phi_j}{\partial z} + \frac{\partial \phi_i}{\partial r} \frac{\partial \phi_j}{\partial r} \right\} \mathrm{d}\Omega$$

$$(S_{33})_{ij} = \int_\Omega \left\{ \frac{\phi_i \phi_j}{r} \right\} \mathrm{d}\Omega, \text{ where } \mathrm{d}\Omega = r \, \mathrm{d}r \, \mathrm{d}z$$

The pressure stiffness matrix, K, and remaining matrices adopt forms

$$K_{ij} = \int_\Omega \nabla \psi_i \nabla \psi_j \, \mathrm{d}\Omega, \quad (L_k)_{ij} = \int_\Omega \psi_i \frac{\partial \phi_j}{\partial x_k} \, \mathrm{d}\Omega, \quad (B_1)_{ij} = \int_\Omega \nabla \phi_i \phi_j \, \mathrm{d}\Omega \qquad (16)$$

Here the notation implies, superscript n denoting the time level, Δt the time step and $\boldsymbol{U}$, $\boldsymbol{U}^*$, $\boldsymbol{P}$, $\boldsymbol{T}$, $\boldsymbol{D}$ the nodal values of velocity, non-solenoidal velocity, pressure, extra-stress and velocity gradient, respectively. A_U, A_2, A_3 are the standard velocity, stiffness and mass matrices. The precise form of A_τ and b_τ varies according to the implementation, and is detailed in Section 3. Galerkin spatial FE discretization is employed within the momentum equation in stage 1, the pressure-correction in stage 2 and the incompressibility constraint in stage 3. The diffusive terms in Equation (3) are treated in a semi-implicit manner in order to enhance stability. The resulting Galerkin mass matrix–vector equations at stages 1 and 3 are solved using an element-by-element Jacobi scheme. The required levels of convergence are attained with only a few Jacobi iterations. A direct Choleski decomposition procedure is invoked to handle stage 2.

The finite volume approach adopted in this work, and applied to stress alone, is of cell-vertex orientation. Cell-vertex schemes, generally maintain their accuracy for broader families of unstructured meshes [21]. The core of these cell-vertex FV schemes is associated with the dictates of fluctuation distribution (FD), governed by FD-coefficients $\{\alpha_l^T\}_{l=1,3}$ on triangular control-volume T; see Reference [3]. These schemes are compact-stencil upwinding techniques. More detail, on the theory and construction of such upwinding schemes, can be found in [3]. They require only the vertices of a triangular cell to evaluate the solution of a given scalar field. The FD-schemes differ based on the appropriate discretization choices for pure advection equation, and upon properties such as conservation, linearity preservation and positivity.

4.1. Fluctuation distribution schemes

Fluctuation distribution schemes can be categorised into those of linear and non-linear types. Both linear and non-linear upwind distribution schemes on unstructured triangular meshes

have been developed over the past years, with built-in properties such as positivity (P) and linearity preservation (LP). Linear schemes can be either P or LP. For both properties to hold, the scheme must be of non-linear form.

4.1.1. Ldb scheme. This is a linearity-preserving (non-positive) scheme defined on each triangle by the angle $\gamma_i^{\ddagger}$ subtended at an inflow vertex by the advection velocity **a** (an average vector per cell). The Ldb distribution coefficients α_l^T, defined per cell node i, may be expressed as

$$
\begin{aligned}
\alpha_i &= (\sin\gamma_1\cos\gamma_2)/\sin(\gamma_1+\gamma_2) \\
\alpha_j &= (\sin\gamma_2\cos\gamma_1)/\sin(\gamma_1+\gamma_2) \\
\alpha_k &= 0
\end{aligned}
\tag{17}
$$

We point out that the closer the advection velocity **a** is to being parallel to one of the cell boundaries, the larger the contribution to the downstream node at that boundary.

4.1.2. Psi scheme. This scheme is non-linear and possesses both positive and linearity preserving characteristics. It is equivalent to the N-scheme with a minmod limiter [8]. The N-scheme is a linear β-scheme, which is positive. It is optimal in the sense that it may use the maximum allowable time-step and the narrowest stencil. The resulting β_i coefficients of the N-scheme, for the case of two inflow sides are:

$$
\begin{aligned}
\beta_i &= -k_i(\phi_i - \phi_k) \\
\beta_j &= -k_j(\phi_i - \phi_k) \\
\beta_k &= 0
\end{aligned}
\tag{18}
$$

where, coefficients k may be expressed as

$$
k_l = \frac{1}{2}\boldsymbol{a}.\boldsymbol{n}_l, \quad \sum_{l=1}^{3}\boldsymbol{n}_l = 0, \quad \sum_{l=1}^{3}k_l = 0
\tag{19}
$$

If we denote the coefficients of the PSI scheme by β_l^* and of the N-scheme by β_l, as in Equation (18), the PSI scheme only deviates from the N-scheme if $\beta_i\beta_j < 0$, and we have

$$
\begin{aligned}
\beta_i^* &= \beta_i - L(\beta_i, -\beta_j) \\
\beta_j^* &= \beta_j - L(\beta_j, -\beta_j)
\end{aligned}
\tag{20}
$$

Here, $L(\mathrm{x,y})$ is the minmod limiter function, defined via the conventional 'sign' operator,

$$
L(x, y) = \tfrac{1}{4}(1 + \mathrm{sign}(xy))(\mathrm{sign}(x) + \mathrm{sign}(y))\min(|x|, |y|)
\tag{21}
$$

---

‡ The equivalent area-weighted version is called LDA-scheme.

4.1.3. Lax–Wendroff (Lax) scheme. This scheme is second order and linear, satisfying linearity-preservation. It is spatially-centred and second-order accurate in space. In addition, it contains a dissipation term designed to control oscillations in the neighbourhood of discontinuities, thus conferring second-order accuracy in time also. For the Lax-scheme, the distribution coefficients α_l^T may be expressed as

$$\alpha_l^T = \frac{1}{3} + \frac{\Delta t}{4\Omega_T}\, \mathbf{a}.\mathbf{n}_l^T \tag{22}$$

where Δt is a time-step size, $\mathbf{a}$ is an averaged advection velocity and n_l^T is a scaled inward-pointing normal vector to an edge of triangle T, opposing node l.

In the current work, we have studied two different viscoelastic flow problems. A model steady problem of sink flow is chosen to analyse consistency and accuracy of the proposed scheme alternatives. In addition, to validate accuracy under more severe settings, a complex problem is investigated, that is, the transient free-surface filament stretching flow. Here, temporal as well as spatial issues must be resolved.

5. SINK FLOW PROBLEM

A steady sink flow problem [22] is solved in two dimensions in the *r-z* plane for an Oldroyd-B fluid. This represents radial sink flow, from the outer radius $r = R_0$ to the inner radius $r = R_i$, with radial velocity component given by $U_r = -(k/r)$ and velocity gradient $\partial U_r/\partial r = k/r^2$, for constant k (see Figure 2). The dominant stress component τ_{rr} in this flow is determined numerically on the basis of frozen kinematics. We adopt a Weissenberg number $We = 0.1$, and polymeric to total-viscosity ratio as $\mu_e/\mu_0 = \frac{8}{9}$. The results obtained are compared with an analytic solution (see Reference [22]):

$$\tau_{rr} = \frac{\mu_e}{\lambda y}\left(1 + C_r e^y\right) \tag{23}$$
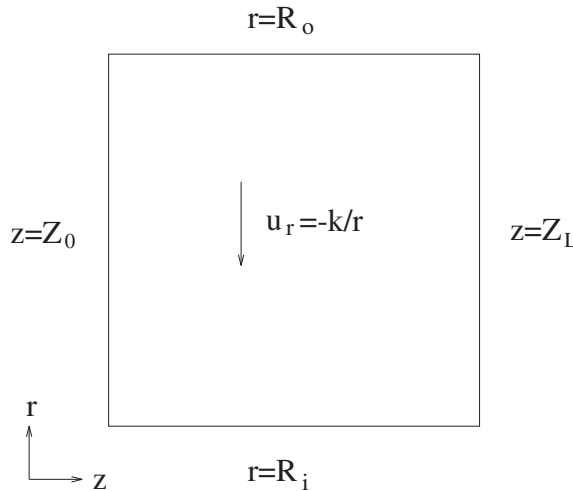
Figure 2. Schematic diagram of two-dimensional sink flow.

where

$$y = \frac{r^2}{2k\lambda} \tag{24}$$

$$C_r = \left(\sigma_{rr} \frac{\lambda Y_0}{\mu_e} - 1 \right) e^{-y_0} \tag{25}$$

Here, σ is the prescribed stress at the outer boundary R_0; $Y_0 = y(R_0)$.

For this model problem, consistency of FV-treatment across source and flux terms is fore-most. Calculations are performed on triangular elements on both structured and unstructured meshes in order to investigate situations with different inflow sides. Through mesh refinement and calibration against an analytical solution, orders of accuracy are established for the various FV-schemes outlined above.

The parameters chosen for this flow problem are: outer radius $R_0 = 2$, inner radius $R_i = 1$ and $k = 2$, implying an inlet velocity $U_r = -1$ at R_0 and outlet velocity $U_r = -2$ at R_i. The axial co-ordinates are taken as $Z_0 = 1$ and $Z_l = 2$. Limiting tolerance to detect convergence is taken as 10^{-8}. The time-step used, is $\Delta t = 0.01$ for 5×5, 10×10 and 10×5 meshes, $\Delta t = 0.005$ for 20×5 and 20×20, and for 40×5 and 40×10 meshes $\Delta t = 0.0025$. The infinity norm $\Delta \tau = \|\tau^h - \tau_{\text{exact}}\|_\infty$, scaled by a maximum value of the exact solution, is reported for compari-son of solutions. To reduce some of the degrees of complexity in the problem, we have chosen to freeze velocity (with analytic gradient) and pressure fields (linearization/localization), so that unequivocally, we may concentrate on accuracy of FV-stress representation (see also, Reference [1]). Boundary conditions for the stress are specified on the inflow boundaries $r = R_0$. For the time-stepping procedure initial conditions are taken as a quiescent state, by default. We note that, σ (R_0) may be set assuming fully-relaxed stress at infinite distance from the sink.

5.1. Results for sink flow

Within the tables of results, we chart the relative difference between analytic and numerical solution, in the infinity norm, on the principle stress component τ_{rr}, over a range of meshes. In this study, the resultant R_T is evaluated in two different forms, either as a boundary integral around Γ_T, as standard,

$$R_T = \oint_{\Gamma_T} \mathbf{R.n} \, d\Gamma_T \tag{26}$$

or, as an area integral,

$$R_T = \int_{\Omega_T} \mathbf{u}.\nabla \tau \, d\Omega \tag{27}$$

These results demonstrate the trends with mesh refinement of the various scheme choices. This provides insight into accuracy attainment for each scheme, that reflects, their spatial convergence rates, reported in terms of $O(h^p)$. We take results in order of structured meshes (see Figure 3), prior to unstructured (see Figure 4). In each instance, we can explore the influence that consistency of implementation has on accuracy. Here, scheme-S1, represents a cell-boundary integral approach, scheme-S2, boundary integral with fixed stress on the bound-aries, and scheme-S3, an area integral procedure.
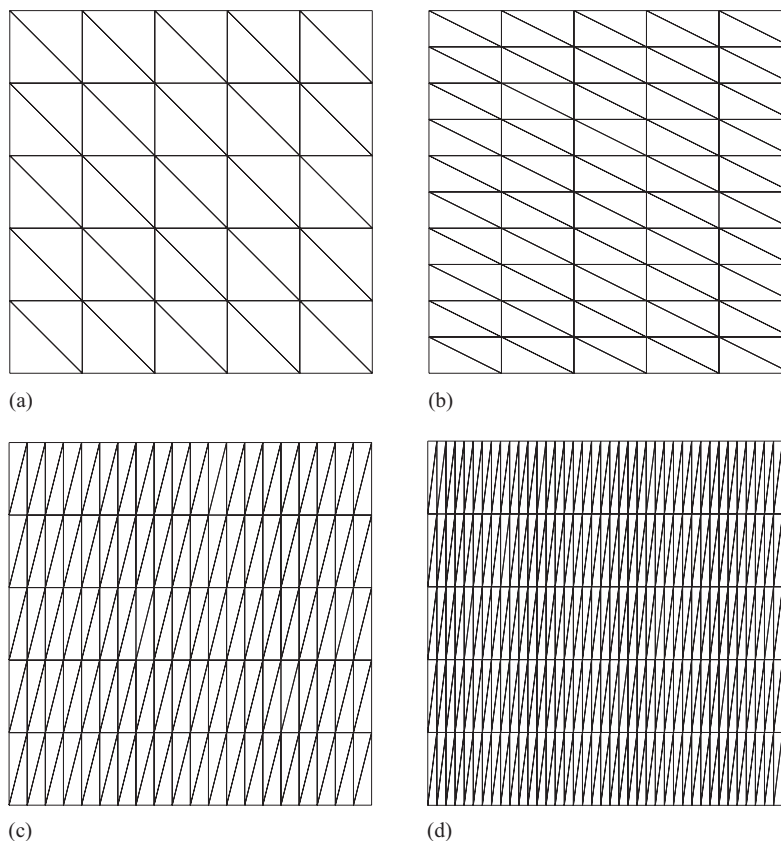
Figure 3. Structured meshes: (a) 5×5; (b) 10×5; (c) 20×5; and (d) 40×5.

5.1.1. Structured mesh solutions. In Figures 5(a)–5(b) and Table I, we compare the consistent (Equation (10)) and inconsistent (Equation (9)) FV formulations. With this set of results, there is only one-inflow side per FV-cell, so that only one node of a triangle will receive an update. This employs therefore a simplistic upwinding treatment. First, we consider scheme-S1, with boundary integral approximation for flux terms. Convergence rates for the consistent implementation are $O(h^{1.5})$ on average, with finer-mesh local-rates tending to $p = 1.1$. The inconsistent counterpart (reflecting the standard version frequently cited in the literature), fairs only slightly less well on average, $O(h^{1.2})$, and closely matches findings on finer meshes. So here, there is not much to choose between these two options, both being around first order in accuracy. The level of error itself is significantly larger with the inconsistent case: by as mush as a factor of four on the finest mesh.

If a uniform fluctuation distribution is adopted, that countermands upwinding with $\alpha_l^T = 1/3$, then similar findings emerge. Here, it is apparent that an mdc treatment of sources is equivalent to a consistent fluctuation distribution approach with uniform coefficients. This is the key to appreciate that accuracy is influenced by other factors than the distribution coefficients alone. Generally, with structured meshes, it is observed that through fluctuation distribution, interior
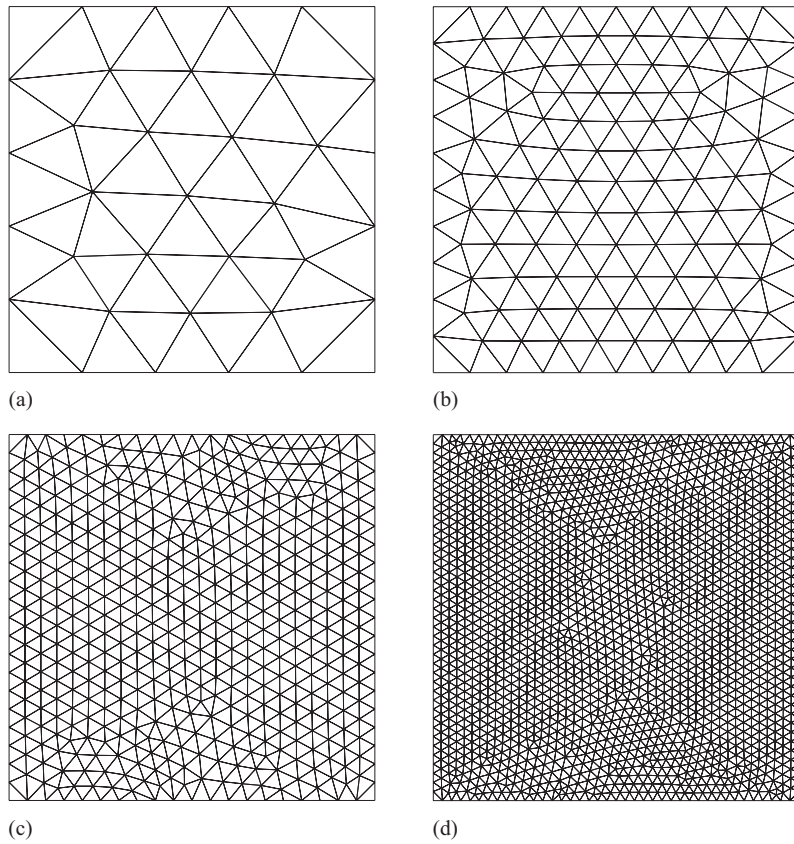
Figure 4. Unstructured meshes: (a) 5×5; (b) 10×10; (c) 20×20; and (d) 40×40.

Table I. $\|\Delta\tau_{rr}\|_\infty$ data, structured meshes, consistent versus inconsistent schemes.

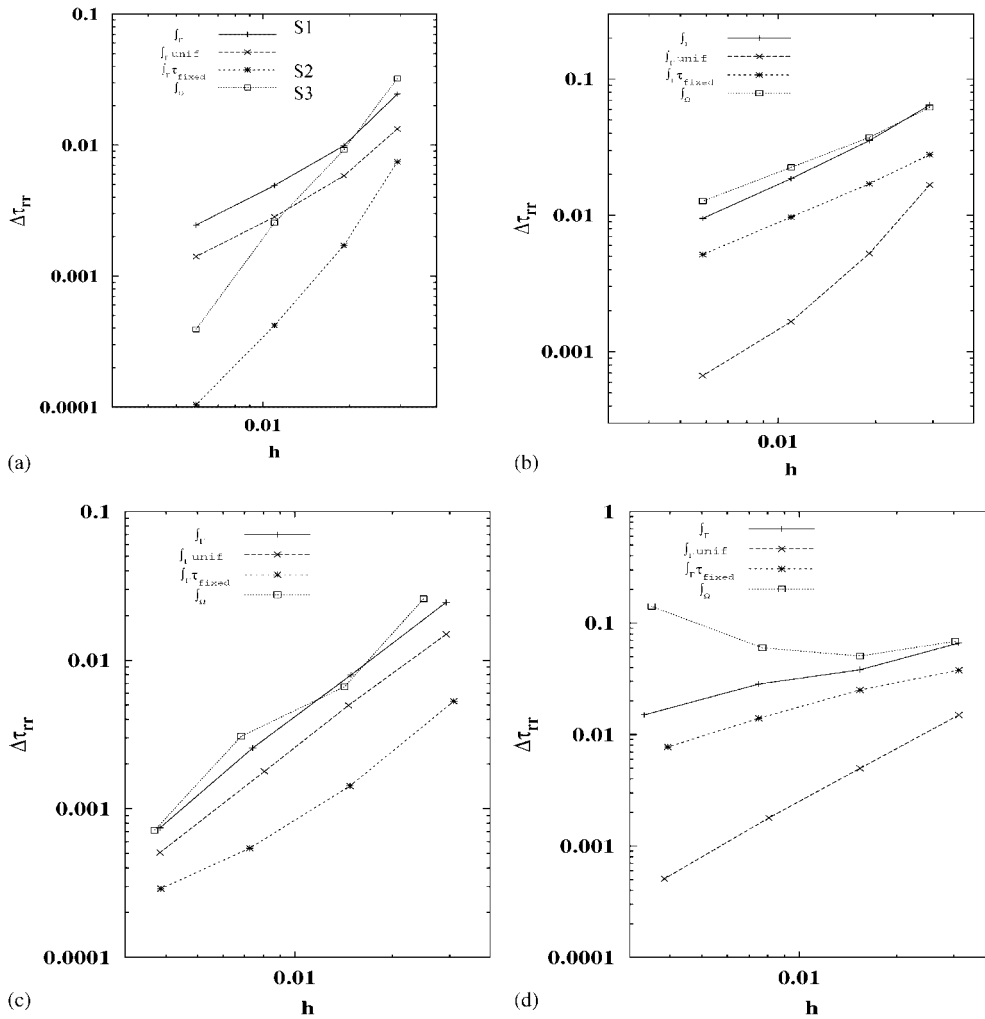| Method/mesh	Consistent		Inconsistent
S1	5×5	0.25×10^{-1}	0.65×10^{-1}
	10×5	0.99×10^{-2}	0.35×10^{-1}
	20×5	0.50×10^{-2}	0.19×10^{-1}
	40×5	0.25×10^{-2}	0.95×10^{-2}
S2	5×5	0.75×10^{-2}	0.28×10^{-1}
	10×5	0.17×10^{-2}	0.17×10^{-1}
	20×5	0.42×10^{-3}	0.97×10^{-2}
	40×5	0.10×10^{-3}	0.52×10^{-2}
S3	5×5	0.32×10^{-1}	0.62×10^{-1}
	10×5	0.92×10^{-2}	0.37×10^{-1}
	20×5	0.26×10^{-2}	0.23×10^{-1}
	40×5	0.39×10^{-3}	0.13×10^{-1}

Figure 5. $\Delta\tau_{rr}$ h-convergence plots for Oldroyd-B; structured meshes: (a) consistent treatment; (b) inconsistent treatment, flux and source, unstructured meshes; (c) consistent treatment; and (d) inconsistent treatment, flux and source. $\int_\Gamma \to S1$; $\int_\Gamma \tau_{\text{fixed}} \to S2$; $\int_\Omega \to S3$.

nodes acquire contributions from an even number of triangles; alternatively, boundary nodes are updated from a single triangle. Therefore, we include results based upon a fixed-stress boundary condition setting, scheme-S2, which always has the effect of reduction in level of error on any fixed meshing choice. With the consistent implementation, we are now able to attain second-order accuracy with mesh refinement, and almost third-order on average. It is apparent, one is losing one order of accuracy here due to the boundary condition issue and lack of balance in the nodal updates with uniform meshing. For the inconsistent counterpart of scheme-S2, first-order accuracy is attained. This is due solely to the inconsistency of treatment between flux (FD) and source terms (on *mdc*).

Table II. $\|\Delta\tau_{rr}\|_\infty$ data: unstructured meshes, consistent versus inconsistent schemes.

Method/mesh		Consistent	Inconsistent
S1	5×5	0.25×10^{-1}	0.66×10^{-1}
	10×10	0.79×10^{-2}	0.38×10^{-1}
	20×20	0.25×10^{-2}	0.28×10^{-1}
	40×40	0.74×10^{-3}	0.15×10^{-1}
S2	5×5	0.53×10^{-2}	0.37×10^{-1}
	10×5	0.14×10^{-2}	0.25×10^{-1}
	20×5	0.54×10^{-3}	0.14×10^{-1}
	40×5	0.29×10^{-3}	0.77×10^{-2}
S3	5×5	0.26×10^{-1}	0.68×10^{-1}
	10×5	0.66×10^{-2}	0.50×10^{-1}
	20×5	0.30×10^{-2}	0.60×10^{-1}
	40×5	0.71×10^{-3}	0.1409

Another aspect that may have a bearing on accuracy is the discrete evaluation of flux, in boundary integral form, and source terms, by area integration. From empirical evidence, it would appear that a close approximation to flux values is gathered at mid-side nodes, whilst sources are well represented at centroid locations. This has lead to the testing of scheme-S3. There instead, fluxes are taken as area integrals, a *non-conservative* representation of the convected term. In consistent form, the average estimate error slope of almost $O(h^3)$ is extracted, with mesh refinement, see Figures 5(a)–5(b). Clearly, this equates to optimal scheme choice. Fixing stress boundary conditions could well improve matters further. However, for general problems, this may not always be plausible. Notably, oncemore the inconsistent counterpart to scheme-S3, is restricted to only first-order accuracy: it is the inconsistency that is responsible for this restriction.

5.1.2. Unstructured mesh solutions. On unstructured meshes and for this model problem, there may be more than one inflow side. Hence, the fluctuation distribution coefficients will vary and nodal updates, by upwinding design, will be distributed to more than one node of each triangle. In this context, considering Ldb as the default, it is meaningful to contrast different fluctuation distribution schemes. In addition, mesh areas will differ from one triangle to another and the number of triangles sharing a node will vary. Hence, nodes throughout the mesh will not be updated in a uniform manner. The results for unstructured meshes are presented in Figures 5(c)–5(d) and Table II.

The main observation that is prominent with unstructured meshes is, there is an order of accuracy lost, in shifting from consistent to inconsistent implementations. Hence, consistency is a dominant issue. Otherwise, there is little to choose between the schemes on average convergence performance, being around $O(h^{1.7})$ for consistent and $O(h^{0.7})$ for inconsistent cases. The exception to the rule is the inconsistent area integral flux evaluation of scheme-S3, that loses h-convergence consistency altogether. Notably, consistent schemes, S1 and S3, both tend to around second-order accuracy with mesh refinement. Also, the influence of upwinding in the departure from structured meshes, has most impact upon consistent scheme S1. Here, this is the only instance where there is improvement in order of accuracy with mesh refinement,

Table III. $\|\Delta\tau_{rr}\|_\infty$ data: unstructured meshes, consistent, Ldb versus Psi.

Method/mesh	Consistent (Ldb)	Consistent (Psi)	
S1	5×5	0.25×10^{-1}	0.24×10^{-1}
	10×10	0.79×10^{-2}	0.78×10^{-2}
	20×20	0.25×10^{-2}	0.25×10^{-2}
	40×40	0.74×10^{-3}	0.74×10^{-3}
S2	5×5	0.53×10^{-2}	0.52×10^{-2}
	10×5	0.14×10^{-2}	0.14×10^{-2}
	20×5	0.54×10^{-3}	0.54×10^{-3}
	40×5	0.29×10^{-3}	0.29×10^{-3}
S3	5×5	0.26×10^{-1}	0.26×10^{-1}
	10×5	0.66×10^{-2}	0.68×10^{-2}
	20×5	0.30×10^{-2}	0.31×10^{-2}
	40×5	0.71×10^{-3}	0.72×10^{-3}

Table IV. $\|\Delta\tau_{rr}\|_\infty$ data: unstructured meshes, consistent versus inconsistent, Ldb, Psi.

Method/mesh	$\alpha_{l(\mathrm{psi})}R + \alpha_{l(\mathrm{ldb})}Q$	$\alpha_{l(\mathrm{ldb})}R + \alpha_{l(\mathrm{psi})}Q$	
S1	5×5	0.25×10^{-1}	0.26×10^{-1}
	10×10	0.73×10^{-2}	0.15
	20×20	0.22×10^{-2}	0.11
	40×40	0.61×10^{-3}	0.11
S2	5×5	0.53×10^{-2}	0.72×10^{-2}
	10×5	0.11×10^{-2}	$0.29 \times 10^{+1}$
	20×5	0.50×10^{-3}	0.12
	40×5	0.21×10^{-3}	0.10
S3	5×5	0.26×10^{-1}	$0.14 \times 10^{+1}$
	10×5	0.44×10^{-2}	$0.18 \times 10^{+1}$
	20×5	0.26×10^{-2}	$0.41 \times 10^{+1}$
	40×5	0.61×10^{-3}	$0.55 \times 10^{+1}$

from $O(h^{1.1})$ for structured, to $O(h^{1.8})$ on unstructured meshes. Interestingly, a choice of uniform fluctuation distribution coefficients with $\alpha_l^T = 1/3$, gives almost identical convergence properties to scheme S1 (the default choice henceforth). This leads one to appreciate that it is the distribution to more than one node that is the critical factor here.

In Table III, the point of attention shifts to the treatment of flux and source terms in respect of fluctuation-distribution schemes. Switching the consistent formulation (10) from Ldb scheme to Psi, we observed an identical error norm slope, to that obtained for the Ldb consistent scheme, see Figures 6(a) and 6(b) with S1. Further, for the evaluation of α_l FD coefficient, we used the Psi scheme for the flux term and Ldb scheme for the source term (Equation (12)). The convergence rate is improved slightly with mesh refinement; see Table IV. This improvement in convergence rate is due to the suitability of the particular
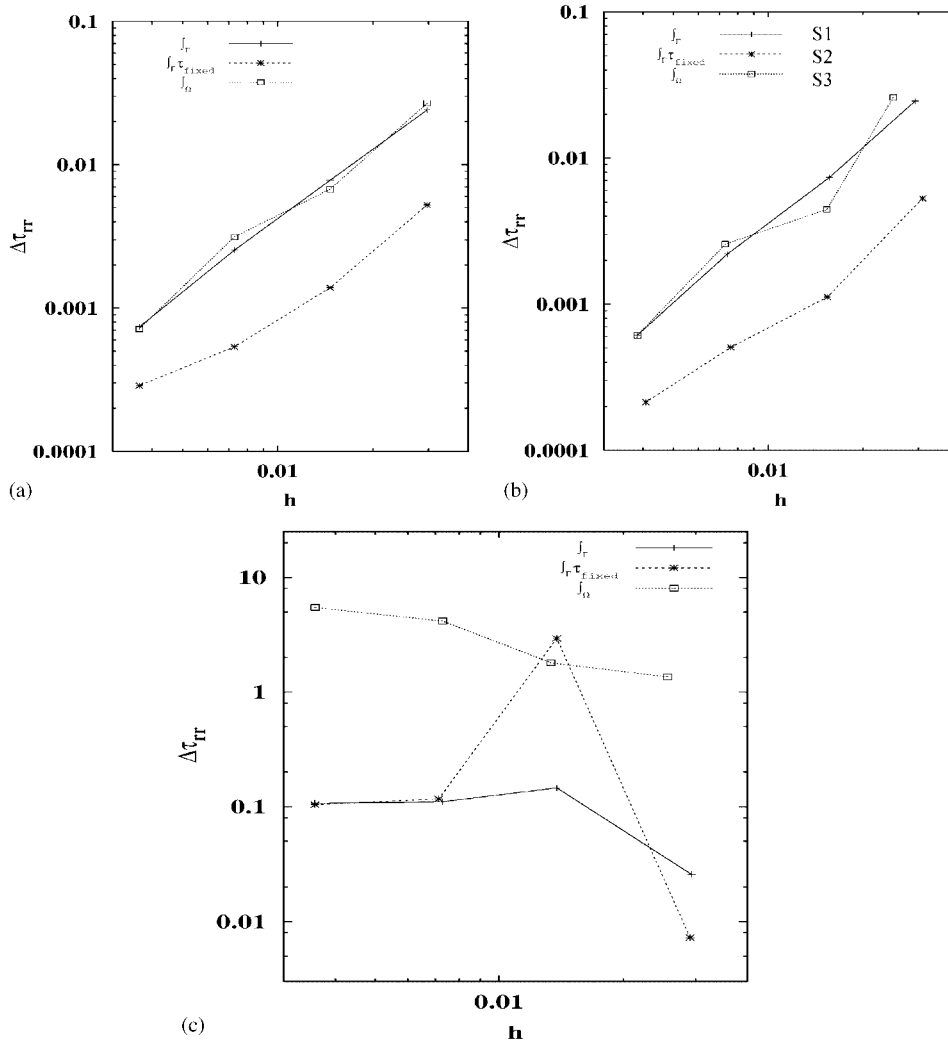
Figure 6. $\Delta\tau_{rr}$ h-convergence plots for Oldroyd-B: unstructured meshes: (a) $\alpha^T_{l(\mathrm{Psi})}(R_T + Q_T)$; (b) $\alpha^T_{l(\mathrm{Psi})}R_T + \alpha^T_{l(\mathrm{Ldb})}Q_T$; and (c) $\alpha^T_{l(\mathrm{Ldb})}R_T + \alpha^T_{l(\mathrm{Psi})}Q_T$ $\int_\Gamma \rightarrow \mathrm{S1}$; $\int_\Gamma \tau_{\mathrm{fixed}} \rightarrow \mathrm{S2}$; $\int_\Omega \rightarrow \mathrm{S3}$.

scheme chosen for each term. The inherited properties of positivity and linearity preserving from the Psi scheme, and linearity preserving property of the Ldb scheme, together retain solution smoothness in temporal (iterative) convergence to steady-state. They do not generate oscillations in the solution, on either coarse or refined meshes, see Figures 7(a)–7(d) with S1, Ldb and Psi annotation. In contrast, when flux terms are computed with the Ldb scheme and source terms with the Psi (positive) scheme (Equation (11)), Figure 6(c) reflects a negative error slope for all schemes, S1–S3, (see Table IV). This is in keeping with expectation, due to the positivity of the Psi scheme, which may introduce fresh extrema in the solution, on both
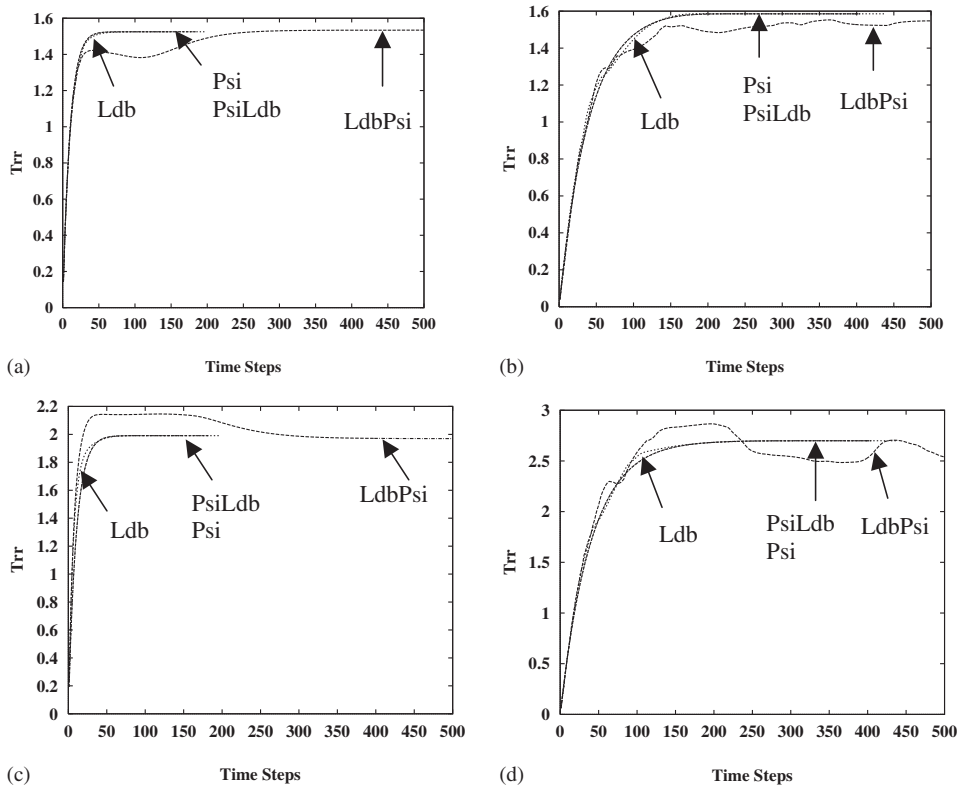
Figure 7. τ_{rr} line plots, unstructured meshes; sampling inlet boundary-node ($r = 1.8$, $z = 0.9$): (a) 5×5 mesh; (b) 40×40 mesh; sampling central-node ($r = 1.5$, $z = 0.5$); (c) 5×5 mesh; and (d) 40×40 mesh, —— PsiLdb; – – – LdbPsi; — — Ldb; - - - - - - - Psi.

coarse and refined meshes (see again, Figures 7(a)–7(d)). Here, under FD-approximation, positivity imposed on source terms (denoted by LdbPsi), degrades solution accuracy. When the Psi scheme is switched onto the flux only, and source retains Ldb treatment (denoted by PsiLdb), this position is rectified. PsiLdb results reflect the smooth time-development of Psi alone.

6. FILAMENT STRETCHING FLOW

In this second section of the study, we consider a complex transient flow with free-surfaces, that described by the extensional deformation of a viscoelastic filament between two coaxial discs. The bottom plate is held fixed and the top-plate is driven in time at an exponential rate providing a constant extension-rate at the filament centre, see Figure 8. It is assumed that inertia and gravity are negligible. The top moving-plate may be set into motion at an
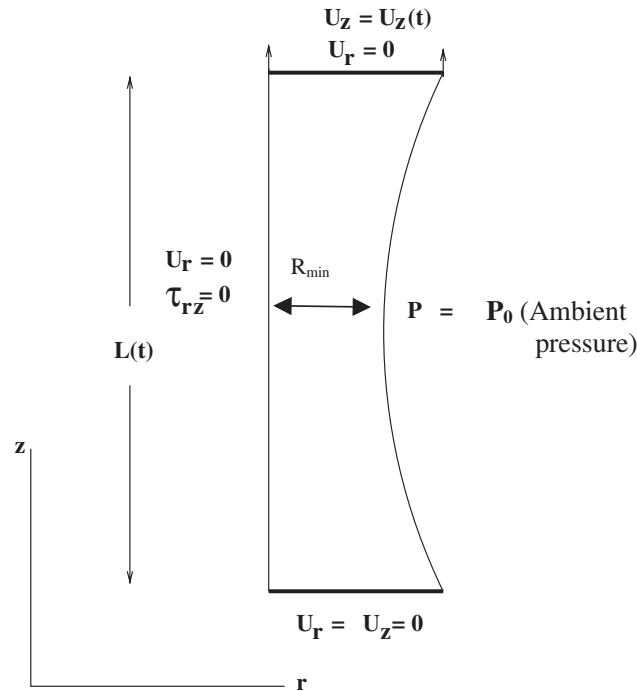
Figure 8. Domain of filament, full-length model with boundary conditions.

exponential rate, so that the dynamic filament-length, $L_P(t)$, may be represented via

$$L_p(t) = L_0 e^{\dot{\varepsilon}_0 t} \tag{28}$$

$$\frac{\mathrm{d}L_p(t)}{\mathrm{d}t} = L_0 \dot{\varepsilon}_0 e^{\dot{\varepsilon}_0 t} \tag{29}$$

where $\dot{\varepsilon}_0$ is an imposed initial stretch-rate and L_0 is the initial length of the filament. The initial aspect ratio of the liquid-bridge is defined as $\wedge_0 = L_0/R_0$, where R_0 is the initial radius. Here, we have selected $\wedge_0 = 1/3$. During elongation, the transient aspect ratio of the liquid bridge may be expressed as $\wedge_0(t) = L_p(t)/R_0$. Material parameters are given as: ρ (density) $=$ $890 \mathrm{kg\, m}^{-3}$, $\dot{\varepsilon}_0$ (stretch-rate) $= 1.6 \mathrm{s}^{-1}$, L_0 (initial length) $= 1.0 \times 10^{-3} \mathrm{m}$, R_0 (initial radius) $=$ $3.0 \times 10^{-3} \mathrm{m}$, χ (surface tension coefficient) $= 28.9 \times 10^{-3} \mathrm{Nm}^{-1}$, μ_0 (zero shear viscosity) $=$ $98 \mathrm{Pa\, s}$.

A rectangular mesh of 20×100 elements, with 8025 nodes and 4000 triangular elements is used to perform the numerical simulation. We choose to scale, length and time, with initial filament length L_0 and initial stretch-rate $\dot{\varepsilon}_0$, respectively. Stress and pressure are scaled by $\mu_0 \dot{\varepsilon}_0$. In addition, we take Weissenberg number, $We = 4$, where now the characteristic velocity, $U = \dot{\varepsilon}_0 L_0$, and $We = De = \lambda_1 \dot{\varepsilon}_0$ and $\lambda_1 = 2.54$ see Reference [19].

The motivation in this part of the study is to advance this hybrid FE/FV methodology and apply the same to complex flow settings. This problem presents a number of challenging aspects including those arising in highly deformed, moving boundary, free-surface transient viscoelastic flows. We establish a favoured fractional-staged solution approach for this flow regime, considering various stress finite volume combinations, namely, inconsistent and consistent FV schemes, pure and hybrid FD-forms (Equations (10)–(12)), and with mdc-inclusion (Equation (13)).

Free-surface computation

The boundary conditions and geometric domain considered within the modeling are illustrated in Figure 8. In addition, initial conditions are taken as quiescent, with exception of on the moving plate, where the initial velocity is taken as $V_0 = (L_0 \varepsilon_0)$. Dirichlet type boundary conditions are imposed on the known parts of the boundary. Continuity of normal and tangential velocities is applied at a fluid–solid interface and continuity of stress at a free-surface [23]. On the free boundary Γ_{fs}, considering an appropriate amount of surface-tension, we impose the dynamic and kinematic boundary conditions outlined below:

The dynamic boundary condition is given *viz.*

$$\boldsymbol{\sigma} . \mathbf{n} = - (p_{\text{ext}} + \chi(R_1^{-1} + R_2^{-1})) . \mathbf{n} \tag{30}$$

Here, $\boldsymbol{\sigma}$ is the Newtonian Cauchy-stress tensor, defined as

$$\boldsymbol{\sigma}_{ij} = - (p \boldsymbol{\delta}_{ij} + 2\mu_0 \mathbf{d}_{ij}) \tag{31}$$

where, χ, $\mathbf{n}$, $\mathbf{d}$ and p_{ext} are the surface tension coefficient, outward unit normal vector to the boundary $\partial \Gamma_{\text{fs}}$, rate-of-deformation tensor and atmospheric pressure, respectively. R_1 and R_2 are the principal radii of curvature of the interface [24, 25], defined functionally through free-surface representation $h(z, t)$,

$$R_1 = \left[\frac{1 + (\partial h / \partial z)^2}{\partial^2 h / \partial z^2} \right]^{3/2}, \quad R_2 = - h \left[1 + \left(\frac{\partial h}{\partial z} \right) \right]^{1/2} \tag{32}$$

The kinematic boundary condition is taken as follows. In order to find the eventual position of the free-surface, we use

$$\frac{\partial h}{\partial t} = u_r - u_z \frac{\partial h}{\partial z}, \quad \forall t \tag{33}$$

In order to retain, smoothness and consistency in surface profiles a Crank–Nicolson treatment (with $\theta = 0.5$) is introduced in discretizing the second-term of r.h.s. of Equation (33), implemented as

$$\frac{\partial h^{t^{n+1}}}{\partial t} = u_r^t - u_z^t \left[\left(\frac{\partial h}{\partial z} \right)^{t^{n-1}} + \theta \left\{ \left(\frac{\partial h}{\partial z} \right)^{t^n} - \left(\frac{\partial h}{\partial z} \right)^{t^{n-1}} \right\} \right] \tag{34}$$

where $0 \leqslant \theta \leqslant 1$. With $\theta = 1$, equation is recovered, to explicit, one-backstep interpretation between t^{n+1} and t^n. For more detail the reader is referred to Reference [20]. Since the flow is incompressible, the free-surface location must satisfy volume conservation.

The kinematic iteration is a natural, separate solution stage for transient free-surface problems. From some initial flow field and domain, the free-surface and moving-boundary is advanced, according to the flow on such boundaries. An updated flow field is calculated and the boundaries advance oncemore, consecutively. At each step the mesh is adjusted so as to comply with kinematic conditions (34), that match the motion of the moving boundaries to the velocity field. The kinematic iteration can be applied to solve a fully-transient problem, or simply to solve a steady state problem. Due to the underpinning boundary conditions and the presence of the free surface, the mesh experiences large deformation both radially (near the interface of the free-surface and the top-plate) and axially. Uniform remeshing is performed radially. For axial remeshing, where the mesh undergoes large stretching, a modified logarithmic (log-sec) remeshing algorithm has been employed, see Reference [26] for details.

6.1. Results and discussion: filament-stretching

6.1.1. Pure FD-schemes. To avoid ambiguity, we begin by discarding mdc-contributions, thus taking $\delta_{\text{mdc}} = 0$. This implies only upwinding constructs are employed (consistently) upon flux (R_T) and source (Q_T) terms, as befits a highly extension-dominated problem. We focus our attention almost entirely upon the distribution of total stress (T_{zz}) and extra-stress (τ_{zz}) along the centreline $(Z = L(t)/2$, see Figure 8). For this problem, total stress is the quantity of physical interest, whilst extra stress is the primary variable computed within the FV-scheme. Here, two cell-vertex fluctuation distribution schemes of interest, Ldb (linear and linearity preserving, second order for steady problems) and Lax–Wendroff (linear, central-scheme with dissipation term, second order) are considered. Such FD-schemes are applied consistently to both flux and source terms as in Equation (10). Along the centreline at $Z = L(t)/2$, and for different finite volume implementations, Plate 1 contrasts the variation of total stress (T_{zz}), whilst Plate 2 conveys the same in extra-stress (τ_{zz}).

With filament stretching, when the plates move apart, free-surface deformation increases, and velocity gradient (D_{zz}) at the mid-point of the free-surface rises sharply towards the free-surface. Hence, the total stress (T_{zz}), elevates in a similar fashion, along the horizontal central axis and a boundary layer develops, as reported in Reference [19]. Due to the presence of the boundary layer, the value of stress drops slightly at the interface node n_1 (see Figures 8 and 9) on the free-surface, when compared to its immediate neighbouring vicinity. In Plate 1, the resulting trend illustrated via the Lax-scheme agrees well with that reported by Yao and McKinley [19]. In addition, a comparison of D_{ZZ} computed with various FV schemes is depicted in Plate 4, contrasted against suitably scaled results from the literature [19]. For this problem, the aspect ratio of the filament is chosen as $\frac{1}{3}$ and $We = 0.5$. It is apparent that the pure FD Lax-scheme outperforms the Ldb and CT3-schemes. In Plate 1, the Ldb-scheme almost replicates that of Lax, albeit with a slight overshoot at the left-hand end of the plot where $r = 0$, and undershoot at the mid-point of the free-surface (node n_1), at the right-hand end of the plot. With the Ldb-scheme, the value of extra-stress at node n_1 vanishes (see Plate 2). The reason for the relatively poor performance of the Ldb-scheme can be attributed to the prevailing direction of the radial velocity profile, U_r. In our previous study on viscous flows [20], we have shown that the flow-field at small Hencky-strains is dominated by the radial velocity, U_r, which is directed inwards at all times. Figure 9 displays the velocity field for the half-length model. In Figure 9(a), the velocity-vectors acting upon the free-surface nodes
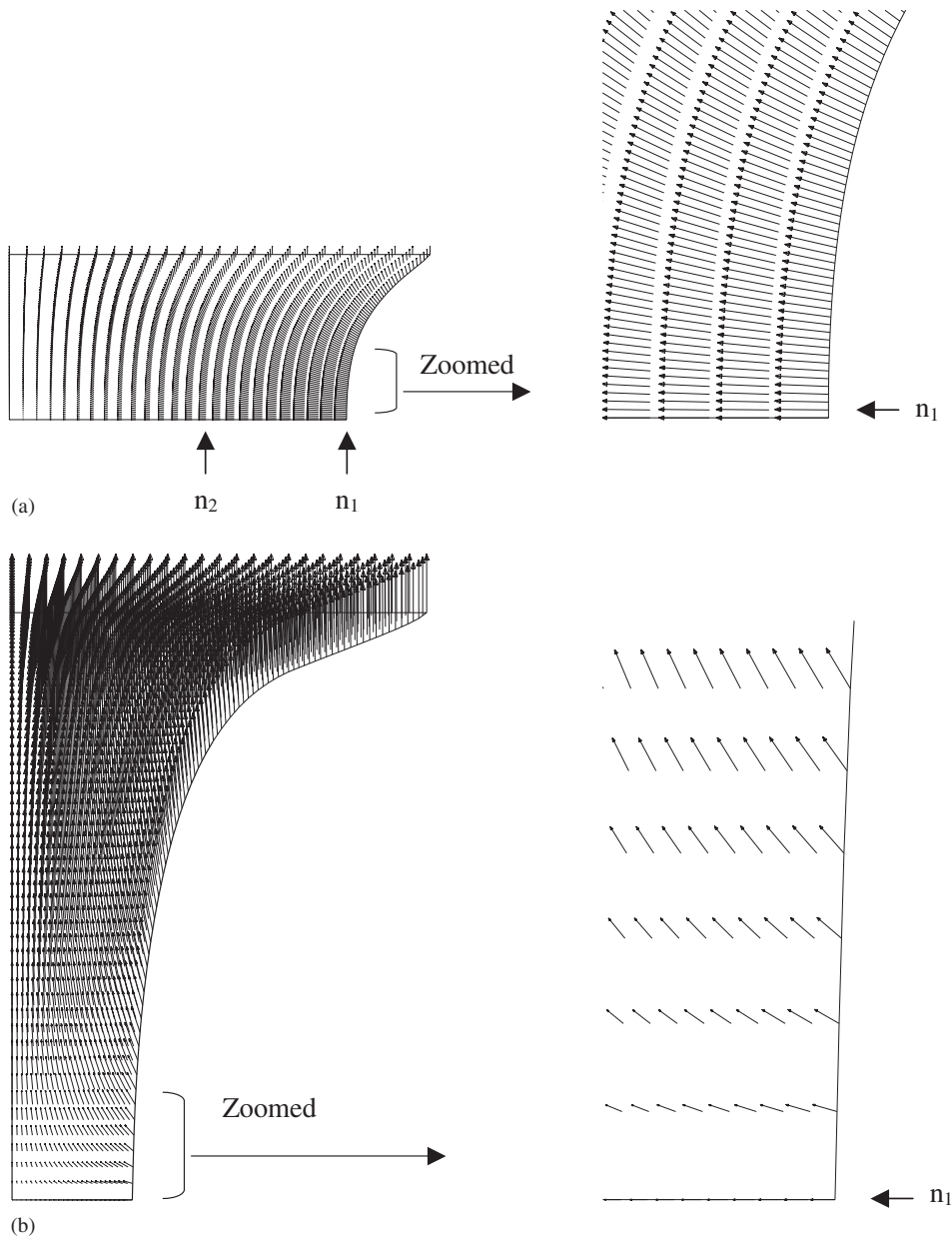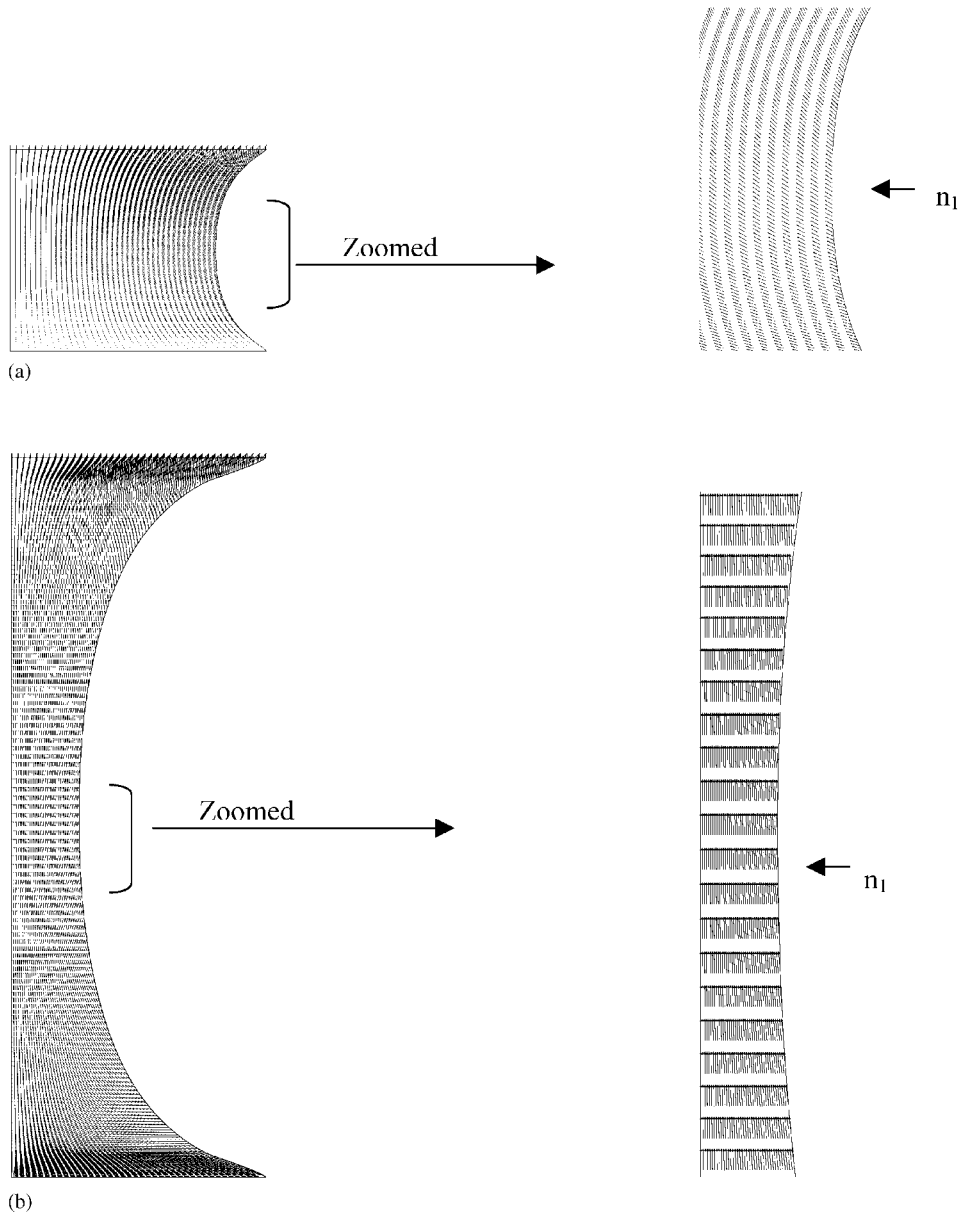
Figure 9. Velocity field: half-length model: (a) $\varepsilon = 0.32$; and (b) $\varepsilon = 1.6$, normal and zoomed views, Newtonian liquid-bridge.

point inwards. Therefore, due to Equation (10), and with the use of a pure upwinding scheme (such as Ldb), it is apparent that nodes on free-surface boundaries will receive no extra-stress contribution whatsoever. This is true for mid-plane node (n_1) at all times, where vanishing axial velocity is imposed in the half-length model problem, see Figure 9(b). This state of

Figure 10. Velocity field: full-length model: (a) $\varepsilon = 0.32$; and (b) $\varepsilon = 1.6$, normal and zoomed views, Newtonian liquid-bridge.

affairs applies equally to the full-length model, see Figure 10(a). The transient evolution of the extra-stress (τ_{zz}) at the crucial node n_1, the mid-point node of the free-surface, is demonstrated in Plate 3a. This figure charts the temporal development of stress over Hencky strain levels from $\varepsilon = 0$ to 0.2. We observe that with the Ldb-scheme, the value of extra-stress

at node n_1, does not shift away from zero. Such discrepancy can be suppressed with recourse to the Lax FD-scheme (Equation (22)), which imparts appropriate contributions to node n_1, as desired. The transient development of extra-stress for an interior node n_2 is depicted in Plate 3b. This node is about half-way along the free-surface mid-plane from node n_1 (on axis $Z = L(t)/2$, see Figure 9(a)). For this node, the Ldb-result mimics the Lax-result closely throughout, and underlines the fact that discrepancy creeps in through upwinding treatment localised to the free-surface interface.

6.1.2. Hybrid FD-schemes. Following our approach for model problems, we have extended our study to include various update strategies of pure FD-form, yet with hybrid combinations. Equation (10) is segregated to allow one FD-scheme to apply to R_T, with a second acting on Q_T; so for example, Psi(R_T)/Ldb(Q_T); Psi(R_T)/Lax(Q_T); Lax(R_T)/Psi(Q_T); Lax(R_T)/Ldb(Q_T); and Ldb(R_T)/Lax(Q_T). Incorporated within Plates 1–3, we are able to contrast results between pure and various hybrid combinations. As above, the transient development of extra-stress (τ_{zz}) at the free-surface mid-plane node (n_1) with various schemes is illustrated in Plate 3(a). A similar plot is provided in Plate 3(b) at internal node (n_2) along the same axis where $Z = L(t)/2$. It is of interest to note that apart from minor oscillations generated by the Lax(R_T)/Psi(Q_T) combination, all fluctuation distribution schemes behave similarly in the interior region of this central plane line, both in space and time (see Plate 2(a) and Plate 3(b)). Discrepancies arise close to the regions at the boundaries (see Plate 2a and Plate 3a). When flux terms are computed via the PSI-scheme and source terms with a Lax-stencil, the solution mimics the consistent pure-FD Lax-scheme, as illustrated in Plate 1(a) and Plate 2(a). In a similar manner, Psi on flux terms and Ldb on source terms, replicates the results from the pure-FD Ldb-scheme. The key element here appears to be the selection of scheme for the source term (Q_T). When the Psi-scheme is invoked for source terms, it introduces discretization error and oscillations result. This is due to the positive character of the Psi-scheme, which may induce fresh extrema in the solution (see above). From the transient development of extra-stress (τ_{zz}) at node n_1 in Plate 3(a), it is conspicuous that in order to have some stress contribution to the boundary node n_1, the scheme of choice on Q_T is that of Lax.

The scheme applied on flux is also important. When one compares Lax(R_T)/Lax(Q_T) versus Ldb(R_T)/Lax(Q_T) in Plate 3(a), the Ldb-version on R_T, generates negatives values for extra-stress at the outset and through the Lax-form on Q_T, the node subsequently gathers contribution in time (solution undershoot results). Note that, with Ldb alone on R_T and Q_T, no contribution to the node n_1 is delivered. It would appear that in the region near the free-surface, both flux and source terms are of comparable strength, and the Ldb-scheme when used on either flux or source, degrades the solution. In contrast, the Psi on R_T with Lax on Q_T, replicates the solution exactly of Lax(R_T)/Lax(Q_T). So positivity via Psi does not detract from R_T-treatment, once Lax is imposed on Q_T, and yields high precision results in contrast to Ldb. This proves the point made earlier on model problems, the essential contribution of positivity upon flux terms, here illustrated through time accuracy (as true for Lax-R_T implementation, also). Furthermore, note that once Lax (Q_T) is replaced with Ldb(Q_T), the Psi(R_T) influence is dominated by the source effect, to the extent that there is now no contribution to extra-stress once again. Hence, pure upwinding performs poorly, on Q_T-terms. Alternatively, the Lax-scheme performs better with Q_T-terms as it is designed to provide second-order accuracy in time for purely convective flows. One notes the structure of the Lax-scheme from Equation

(22) and the perturbation form about the uniform $\frac{1}{3}$-weighting (hence, not purely upwinding by definition).

6.1.3. Schemes with mdc-inclusion. Elsewhere for complex flows, mdc-contributions have been found to ensure numerical stability and accuracy for both steady and transient problems [1, 11, 12]. With mdc inclusion, the scheme employed here is CT_3, the more consistent form with $\delta_{\text{mdc}} = 1 - \delta_t$ [11]. In the present transient problem, from Plate 1(a) and Plate 2(b), it is apparent that the inclusion of mdc degrades the solution. The inclusion of mdc-contributions diffuses the solution (see Plate 2(b)). The discrepancy is greater at the free-surface and the central region, where the velocity gradient D_{zz}, rises sharply from a constant value to a peak, as demonstrated in Plate 4. In the regions where such sharp change in gradient occurs, the strength of the source terms can be high and the flow can be heavily convective in nature. The adjustment in direction of flow is apparent in the velocity vectors in Figure 9. Hence, fluctuation distribution alone is superior to only mdc-inclusion. The inclusion of mdc introduces significant error in the transient stress evolution at the free-surface node n_1, and the internal node n_2, as demonstrated in Plates 3(a) and 3(b). The value of extra-stress at the free-surface node n_1, is always negative with mdc-inclusion. Plate 1(b) contrasts Lax and Ldb implementations, both with mdc-inclusion (CT_3). Here, the linearity preserving property of Ldb preserves greater smoothness in the solution. Nevertheless, mdc-inclusion is clearly responsible for greater injection of error in the solution, irrespective of Lax or Ldb choice. In addition, we have considered variants of the standard inconsistent ($\alpha R_T + Q_{\text{mdc}}$) scheme, and ($\alpha R_T + \delta_T Q_T + \delta_{\text{mdc}} Q_{\text{mdc}}$)-scheme. Here, R_T is of Lax-form. The results are displayed in Plate 1(b) and Plate 2(b), from which it is conspicuous that for this problem, any form of mdc-inclusion, degrades the solution, irrespective of whether this is imparted to source terms alone or with flux terms, consistently or inconsistently. Curiously, the standard implementation (S1) does provide the most damping to the interior solution profile in Plate 1(b).

7. CONCLUSION

For model problems, consistent formulation of the flux and source terms has been found to improve the accuracy to almost a third order. The precise choice of a FD-scheme for the flux and source terms is the key issue, in attaining such higher orders of accuracy. An inappropriate choice would detract from this position. In shifting from structured to unstructured meshes, one order of accuracy is lost. Through the study of various FV-scheme choices upon a well-characterized model problem, we have been able to pinpoint some of the key issues that must be addressed in accurately discretizing viscoelastic flow equations. The principle issue has been the consistent incorporation of non-trivial source terms within a standard FV cell-vertex formulation. Overall, we conclude for model flows, that consistency of approach is vital to attain the higher levels of accuracy, be this on structured or unstructured meshes. Under optimal selection, this may yield a third-order of accuracy on structure meshes and second order on unstructured alternatives. In contrast, for standard approaches, such as inconsistent scheme S1 (commonly quoted in the literature), we have illustrated how a significant loss of accuracy may be incurred. The consequence is restriction to first-order accuracy. This may give rise to other, knock-on effects in the accurate resolution of more complex, highly-elastic flows.

In the study of complex problems under filament-stretching flows, we have demonstrated improved levels of accuracy achieved with a Lax-scheme. This is so, in contrast to a counterpart Ldb-implementation, reported at small Hencky-strain levels. Here, we have been able to isolate the shortcomings of these upwinding schemes, whilst dealing with such transient free-surface problems. We observe that the velocity-field in these filament-stretching flows with liquid-bridges imposes certain restrictions on the upwinding scheme approximations for these to perform well in the presence of free-surfaces. An optimal choice has been proposed, having contrasted results for pure fluctuation distribution schemes, various hybrid combinations, and with mdc-inclusion. We summarise our main conclusions. First, mdc-inclusion is not recommended for such transient extension-dominated problems with contact-line/interfaces, as it degrades accuracy. High accuracy is achieved via the use of the second-order Lax-scheme. The optimal choice for such transient contact-line/interface problems is Lax on Q_T; on R_T, Lax or Psi. Application of positive schemes on Q_T degrades the solution for both model and complex problems. We have been able to achieve a high degree of precision on velocity gradients with pointwise estimation, even accommodating contact-line/interfaces. The results obtained with the optimum scheme, agree well with counterpart finite element solutions available in the open literature.

REFERENCES

1. Wapperom P, Webster MF. Simulation for viscoelastic flow by a finite volume/element method. *Computer Methods in Applied Mechanics and Engineering* 1999; **180**:281–304.
2. Darwish MS, Whiteman JR. Numerical modelling of viscoelastic liquids using finite-volume method. *Journal of Non-Newtonian Fluid Mechanics* 1992; **45**:311–337.
3. Hubbard ME, Roe PL. Multidimensional upwind fluctuation distribution schemes for scalar time dependent problems. *International Journal for Numerical Methods in Fluids* 2000; **33**:711–736.
4. Morton KW, Crumpton PI, Mackenzie JA. Cell-vertex methods for inviscid and viscous flows. *Computers and Fluids* 1993; **22**:91–102.
5. Crumpton PI, Mackenzie JA, Morton KW. Cell-vertex algorithms for the compressible Navier–Stokes equations. *Journal of Computational Physics* 1993; **109**:1–15.
6. Morton KW, Rudgyard MA, Shaw GJ. Upwind iteration methods for the cell vertex scheme in one dimension. *Journal of Computational Physics* 1994; **114**:209–226.
7. Berzins M, Ware JM. Positive cell-centered finite volume discretization methods for hyperbolic equations on irregular meshes. *Applied Numerical Methods* 1995; **16**:417–438.
8. Struijs R, Deconinck H, Roa PL. Fluctuation splitting for the 2D Euler equations. *Technical Report Series*, von Karman Institute of Fluid Dynamics, 1991.
9. Sato T, Richardson SM. Explicit numerical simulation of time-dependent viscoelastic flow problems by finite element/finite volume method. *Journal of Non-Newtonian Fluid Mechanics* 1994; **51**:249–275.
10. Brooks AN, Hughes JR. Streamline upwind/Petrov–Galerkin formulations for convection dominated flows with particular emphasis on the incompressible Navier–Stokes equations. *Computer Methods in Applied Mechanics and Engineering* 1982; **32**:199–259.
11. Aboubacar M, Webster MF. Development of an optimal hybrid finite volume/finite element method for viscoelastic flows. *International Journal for Numerical Methods in Fluids* 2003; **41**:1147–1172.
12. Webster MF, Tamaddon-Jahromi HR, Aboubacar M. Transient viscoelastic flows in planar contractions. *Journal of Non-Newtonian Fluid Mechanics* 2003; in press.
13. Matallah H, Townsend P, Webster MF. Recovery and stress-splitting schemes for viscoelastic flows. *Journal of Non-Newtonian Fluid Mechanics* 1998; **75**:139–166.
14. Wapperom P, Webster MF. A second-order hybrid finite-element/volume method for *viscoelastic flows*. *Journal of Non-Newtonian Fluid Mechanics* 1998; **79**:405–431.
15. Tirtaatmadja V, Sridhar T. A filament stretching device for measurement of extensional viscosity. *Journal of Rheology* 1993; **37**:1081–1102.
16. Yao M, McKinley GH, Debbaut B. Extensional deformation, stress relaxation and necking failure of viscoelastic filaments. *Journal of Non-Newtonian Fluid Mechanics* 1998; **79**:469–501.

17. Sizaire R, Legat V. Finite element simulation of a filament stretching extensional rheometer. *Journal of Non-Newtonian Fluid Mechanics* 1997; **71**:89–107.
18. Rasmussen HK, Hassager O. Three-dimensional simulations of viscoelastic instability in polymeric filament. *Journal of Non-Newtonian Fluid Mechanics* 1999; **82**:189–202.
19. Yao M, McKinley GH. Numerical simulation of extensional deformations of viscoelastic liquid bridges in filament stretching devices. *Journal of Non-Newtonian Fluid Mechanics* 1998; **74**:47–88.
20. Chandio MS, Matallah H, Webster MF. Numerical simulation of viscous filament-stretching flows. *International Journal for Numerical Methods in Heat Fluid Flow* 2003; **13**(7):899–930.
21. Hirsh c. *Numerical Simulations of Internal and External Flows*, vol. 2. Wiley: New York, 1990.
22. Gunter S, Townsend P, Webster MF. The simulation of some model viscoelastic flows. *International Journal for Numerical Methods in Fluids* 1996; **23**:691–710.
23. Fourcade E, Bertrand F, Reglat O, Tanguy PA. Finite element analysis of fluid-solid interaction in the metering nip of a metering size press. *Computer Methods in Applied Mechanics and Engineering* 1999; **174**:235–245.
24. Tanguay P, Fortin M, Choplan L. Finite element simulation of dip coating, I: Newtonian Fluids. *International Journal for Numerical Methods in Fluids* 1984; **4**:441–457.
25. Keunings R. An algorithm for the simulation of transient viscoelastic flows with free surfaces. *Journal of Computational Physics* 1986; **20**:209–226.
26. Kröger R, Berg S, Delgado A, Rath HJ. A stretching behaviour of large polymeric and Newtonian liquid bridges in plateau simulation. *Journal of Non-Newtonian Fluid Mechanics* 1992; **45**:385–400.
27. Oldroyd JG. On the formulation of rheological equations of state. *Proceedings of the Royal Society* 1950; **A200**:523–541.
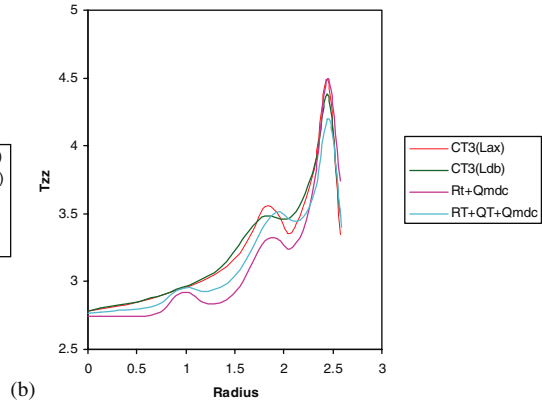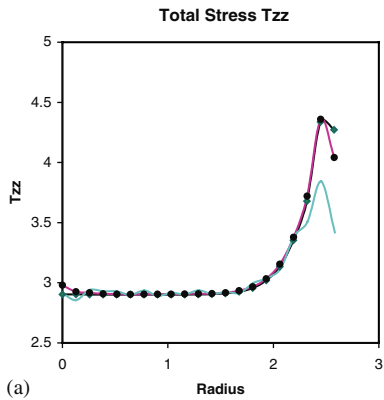
Plate 1. Total stress T_{zz}, along centre-line $Z = L(t)/2$, $We = 4$, initial aspect ratio $\wedge_0 = \frac{1}{3}$: (a) various FD-schemes; and (b) mdc-inclusion.
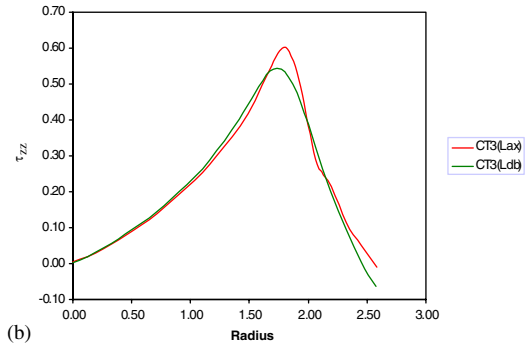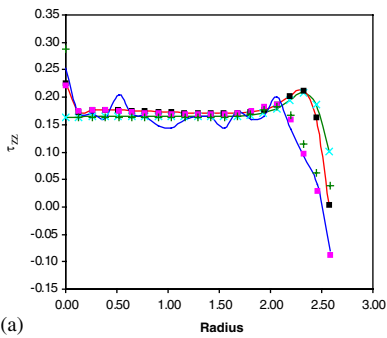

Plate 2. Extra-stress T_{zz} along centre-line at $Z = L(t)/2$, $We = 4$, initial aspect ratio $\wedge_0 = \frac{1}{3}$: (a) pure and hybrid fluctuation distribution FV- schemes; and (b) mdc-inclusion.
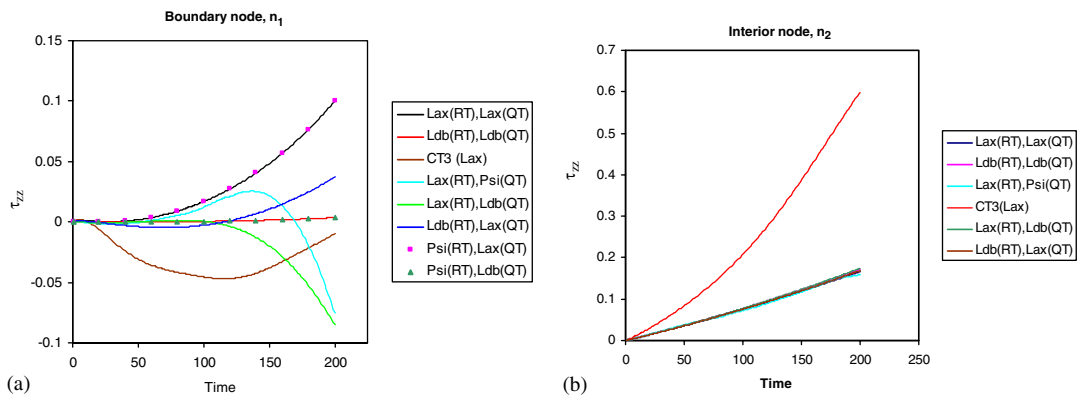
Plate 3. Transient development of extra-stress τ_{zz}, $\varepsilon = 0$ to 0.2: (a) node n_1; and (b) node n_2.
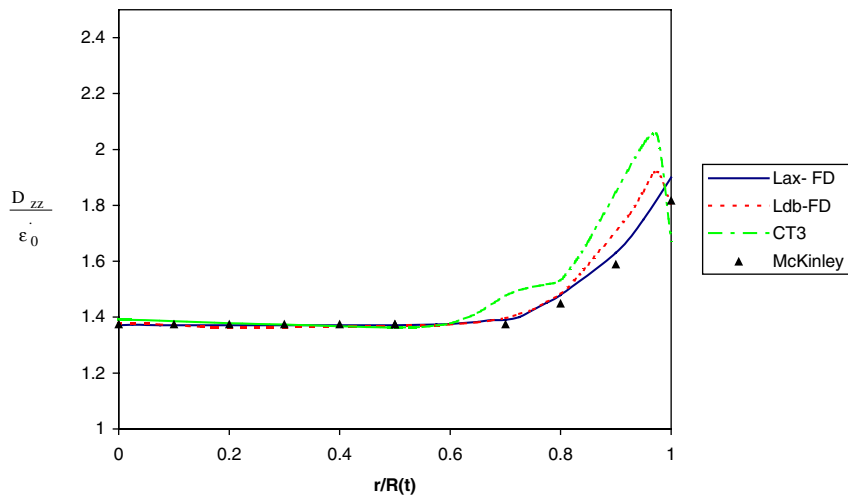

Plate 4. Comparison of D_{zz} along $Z = L(t)/2$, various schemes versus literature, initial aspect ratio $\wedge_0 = \frac{1}{3}$, $We = 0.5$.